

A localised subgrid scale model for fluid dynamical simulations in astrophysics II: Application to type Ia supernovae

W. Schmidt^{1,2}, J. C. Niemeyer¹, W. Hillebrandt², and F. K. Röpke²

¹ Lehrstuhl für Astronomie, Institut für Theoretische Physik und Astrophysik, Universität Würzburg, Am Hubland, D-97074 Würzburg, Germany

² Max-Planck-Institut für Astrophysik, Karl-Schwarzschild-Str. 1, D-85741 Garching, Germany

Received / Accepted

Abstract. The dynamics of the explosive burning process is highly sensitive to the flame speed model in numerical simulations of type Ia supernovae. Based upon the hypothesis that the effective flame speed is determined by the unresolved turbulent velocity fluctuations, we employ a new subgrid scale model which includes a localised treatment of the energy transfer through the turbulence cascade in combination with semi-statistical closures for the dissipation and non-local transport of turbulence energy. In addition, subgrid scale buoyancy effects are included. In the limit of negligible energy transfer and transport, the dynamical model reduces to the Sharp-Wheeler relation. According to our findings, the Sharp-Wheeler relation is insufficient to account for the complicated turbulent dynamics of flames in thermonuclear supernovae. The application of a co-moving grid technique enables us to achieve very high spatial resolution in the burning region. Turbulence is produced mostly at the flame surface and in the interior ash regions. Consequently, there is a pronounced anisotropy in the vicinity of the flame fronts. The localised subgrid scale model predicts significantly enhanced energy generation and less unburnt carbon and oxygen at low velocities compared to earlier simulations.

Key words. Stars: supernovae: general – Hydrodynamics – Turbulence – Convection – Methods: numerical

1. Introduction

For supernovae of type Ia, Hoyle & Fowler (1960) proposed a thermonuclear runaway initiated in C+O white dwarfs close to the Chandrasekhar limit as the cause of the explosion. Since the original proposal, there has been vivid controversy of how such an explosion might come about and what the exact physical mechanism could be. Today the computational facilities to process three-dimensional large-eddy simulations (LES) of the explosion event are available. Remarkably, these powerful means have not aided in arriving at a consensus yet. The disagreement stems from some crucial questions. Firstly, what is the appropriate flame speed model? Secondly, does the explosion completely proceed as a deflagration, or does a transition to a delayed detonation set in at some point? The deflagration to detonation transition (DDT) proposed by Khokhlov (1991) and Woosley & Weaver (1994) appears to resolve the drawbacks of the pure deflagration model. In particular, the energy output obtained from simulations with artificial DDT is closer to the observed one, and less carbon and oxygen is left behind (Gamezo et al. 2004, 2005; Golombek & Niemeyer 2005). For the theoretical understanding of thermonuclear supernovae, however, the lack of a convincing explanation for the initiation of the transition is unsatisfactory (Khokhlov et al. 1997; Niemeyer & Woosley 1997;

Niemeyer 1999; Zingale et al. 2005). In the aforementioned numerical models, a DDT is artificially triggered at more or less arbitrary instants of time.

As for the flame speed model, the controversy is whether subgrid scale (SGS) turbulence is mostly driven by Rayleigh-Taylor instabilities or dominated by the energy transfer through the turbulence cascade. The former point of view holds that the magnitude of SGS velocity fluctuations v' is basically given by the Sharp-Wheeler relation (Davies & Taylor 1950; Sharp 1984)

$$v_{\text{RT}}(l) = 0.5 \sqrt{lg_{\text{eff}}} \quad (1)$$

where $v_{\text{RT}}(l)$ is the asymptotic rise velocity of a perturbation of size l due to buoyancy. The effective gravity g_{eff} is determined by the density contrast at the interface between burned and unburned material. Setting the turbulent flame speed equal to $v_{\text{RT}}(\Delta)$, where Δ is the resolution of the numerical grid, has been used in some simulations of type Ia supernovae (Gamezo et al. 2003; Calder et al. 2003; Gamezo et al. 2004). However, simple scaling arguments disfavour this proposition (Niemeyer & Hillebrandt 1995; Niemeyer & Kerstein 1997). Assuming that non-linear interactions between turbulent eddies of different size l set up a Kolmogorov spectrum, the root mean square turbulent velocity fluctuations obey the scaling law $v'(l) \propto l^{1/3}$. Since the Sharp-Wheeler relation implies

$\nu_{\text{RT}}(l) \propto l^{1/2}$, we have $\nu_{\text{RT}}(l)/\nu'(l) \propto l^{1/6} \rightarrow 0$ towards decreasing length scales. Consequently, Niemeyer & Hillebrandt (1995) adopted a SGS model based on the dynamical equation for the turbulence energy k_{sgs} , i.e. the kinetic energy of unresolved velocity fluctuations (Schumann 1975). The major weakness of their approach arises from the fairly tentative closures which were formulated *ad hoc* for LES of stellar convection (Clement 1993).

Various refutations of the scaling argument have been put forward. To begin with, the spectrum of turbulence energy might be different from the Kolmogorov spectrum. However, recent direct numerical simulations support the hypothesis of a Kolmogorov spectrum in buoyancy-driven turbulent combustion (Zingale et al. 2005). A more serious concern is that there might be not enough time to reach the state of developed turbulence with a Kolmogorov spectrum in the transient scenario of a supernova explosion. This question is difficult to settle *a priori*. For this reason, we took an unbiased point of view and accommodated buoyancy effects in the form of an Archimedian force term in the SGS turbulence energy model.

In contrast to the previously used SGS turbulence energy model, the new localised model which is thoroughly discussed in paper I neither presumes isotropy nor a certain turbulence energy spectrum function. This is possible by virtue of a dynamical procedure for the determination of the SGS eddy-viscosity $\nu_{\text{sgs}} = C_\nu \Delta k_{\text{sgs}}^{1/2}$ which was adapted from Kim et al. (1999). Furthermore, we apply the co-expanding grid introduced by Röpke (2005). The growth of the cutoff length Δ due to the grid expansion poses a challenge for the SGS model because of the partitioning between resolved energy and SGS energy changes in time. We will show that this rescaling effect can be taken into account by utilising the dynamical procedure for the calculation of eddy-viscosity parameter C_ν . The rescaling algorithm as well as the computation of the Archimedian force is explained in Sect. 2, followed by the discussion of results from three-dimension numerical simulations in Sect. 3. It is demonstrated that the newly proposed SGS model substantially alters the predictions of the deflagration model. In particular, we will analyse the significance of SGS buoyancy affects.

2. The flame speed model

For the relation between the turbulent flame speed s_t and the SGS turbulence velocity q_{sgs} , we adhere to the results found by Pocheau (1994) from a theoretical analysis and set

$$s_t = s_{\text{lam}} \sqrt{1 + C_t \left(\frac{q_{\text{sgs}}}{s_{\text{lam}}} \right)^2}, \quad (2)$$

where $C_t = 4/3$. In the asymptotic regime of turbulent burning, $s_t \approx 2q_{\text{sgs}}/\sqrt{3}$ which is consistent with Peters (1999).

The evolution of q_{sgs} is given by a non-linear partial differential equation which is obtained by dividing the equation for the specific SGS turbulence energy $k_{\text{sgs}} = \frac{1}{2}q_{\text{sgs}}^2$ (see Sect. 3 of part I) by q_{sgs} . For turbulence driven by the Rayleigh-Taylor instability, an additional source term stems from buoyancy effects on subgrid scales. This Archimedian force, which is proportional to the effective gravity due to the density contrast between nuclear fuel and ash, directly induces turbulent velocity

fluctuations. The form of the Archimedian force will be proposed in Sect. 2.1. Moreover, the Eulerian time derivative must account for the rescaling of the turbulence energy due to the temporal shift of the cutoff length. We will denote the partial derivative with respect to the rescaled quantities by ∂^* . The Lagrangian time derivative thus becomes

$$\frac{D^*}{Dt} = \frac{\partial^*}{\partial t} + \mathbf{v} \cdot \nabla. \quad (3)$$

The complete dynamical equation for the SGS turbulent velocity is

$$\begin{aligned} \frac{D^*}{Dt} q_{\text{sgs}} - \frac{1}{\rho} \nabla \cdot (\rho \ell_\kappa q_{\text{sgs}} \nabla q_{\text{sgs}}) - \ell_\kappa |\nabla q_{\text{sgs}}|^2 \\ = \frac{1}{\sqrt{2}} C_A g_{\text{eff}} + \ell_\nu |S^*|^2 - \frac{7}{30} q_{\text{sgs}} d - \frac{q_{\text{sgs}}^2}{\ell_\epsilon}. \end{aligned} \quad (4)$$

The rate-of-strain scalar $|S^*|$ is defined by $|S^*|^2 = 2S_{ij}^* S_{ij}^*$, where S_{ij}^* is the trace-free part of the symmetrised Jacobian matrix of the velocity field, $S_{ij} = \frac{1}{2}(\partial_j v_i + \partial_i v_j)$, and $d = S_{ii} = \partial_i v_i$ is the divergence. The characteristic length scales ℓ_κ , ℓ_ν and ℓ_ϵ are related to SGS turbulent transport, the rate of energy transfer from resolved toward subgrid scales and the rate of viscous dissipation. Each characteristic length can be expressed in terms of the effective cutoff length Δ_{eff} and a similarity parameter:

$$\ell_\nu = \frac{C_\nu \Delta_{\text{eff}}}{\sqrt{2}}, \quad \ell_\epsilon = \frac{2\sqrt{2}\Delta_{\text{eff}}}{C_\epsilon}, \quad \ell_\kappa = \frac{C_\kappa \Delta_{\text{eff}}}{\sqrt{2}}. \quad (5)$$

For the determination of the closure parameters C_ν , C_ϵ and C_κ see Sect. 4 of part I. The advection of q_{sgs} by the resolved flow is computed with the piece-wise parabolic method (Colella & Woodward 1984). Due to the dissipative effects of this numerical scheme on the smallest resolved length scales, we set $\Delta_{\text{eff}} \approx 1.6\Delta$ (Schmidt et al. 2005b). The diffusion terms on the left hand side of equation 4 is computed by means of fourth order centred differences, and for the source term on the right-hand side a semi-implicit Adams-Moulton method is used. In the remainder of this section, we describe the calculation of the SGS Archimedian force and the rescaling procedure.

2.1. Archimedian production

There has been an ongoing debate whether the production of SGS turbulence is dominated by the buoyancy of SGS perturbations in the interface between ash and fuel or by eddies produced through the turbulence cascade. In the first case, the source of energy is the gravitational potential energy, whereas non-linear transfer supplies kinetic energy from larger scales in the second case. In general, it is quite difficult to separate the energy injection caused by gravity in wave number space because gravitational effects are genuinely non-local. For Rayleigh-Taylor driven turbulence, however, we know the simple Sharp-Wheeler scaling relation (1) which provides an algebraic closure for the Archimedian force density Γ_{sgs} introduced in Sect. 3 of part I. Therefore, we propose a novel approach which combines both the production of SGS turbulence

through the cascade and the Rayleigh-Taylor mechanism in the dynamical equation for q_{sgs} .

Because Γ_{sgs} has the dimension of an acceleration times velocity, we interpret this term as the product of a specific *Archimedian force* and the SGS turbulence velocity q_{sgs} . This means the following: In any finite-volume cell those portions of the fluid with density less than the smoothed density ρ will experience buoyancy relative to the other portions of higher density in the mean gravitational field. In subsonic turbulent flows, the small random density fluctuations caused by compression and rarefaction are expected to produce very little net buoyancy. However, a special situation is encountered in the cells intersected by the flame fronts. Since the flames are far from being completely resolved in numerical simulations of SNe Ia, the substructure of the front in combination with the density gradient across the front will produce SGS buoyancy. Equivalently, one can think of perturbations in the flame front on length scales $\lambda_{\text{fp}} \lesssim l \lesssim \Delta$ as being Rayleigh-Taylor unstable and producing SGS turbulence. The *fire polishing length* λ_{fp} then marks the lower threshold for perturbations to grow (see Zingale et al. 2005). Once turbulence has developed, λ_{fp} can be identified with the Gibson length l_G , i.e. the smallest length scale on which the flame propagation is affected by turbulent eddies. Perturbations of size $l \gtrsim \Delta$, on the other hand, set fluid into motion on numerically resolved length scales. But the transfer of energy through the turbulence cascade eventually produces SGS turbulence as well. This production channel corresponds to the term Σ_{sgs} in the equation for the SGS turbulence energy (see sect 3 of part I).

The Archimedian force generated by the density gradient across flame fronts is given by the effective gravity

$$g_{\text{eff}} = \text{At } g, \quad (6)$$

where the Atwood number

$$\text{At} = \frac{\rho_{\text{f}} - \rho_{\text{b}}}{\rho_{\text{f}} + \rho_{\text{b}}} \quad (7)$$

is a measure for the density contrast between burned material and nuclear fuel. In the vicinity of the flame front, the lowest order estimate for the SGS buoyancy term is $\Gamma_{\text{sgs}} \sim \rho q_{\text{sgs}} g_{\text{eff}}$, provided that $\Delta \gtrsim \lambda_{\text{fp}}$. If Δ becomes smaller than λ_{fp} , SGS perturbations in the flame front are not subject to the RT-instability and Γ_{sgs} vanishes. In conclusion, we propose the following closure:

$$\Gamma_{\text{sgs}} = \frac{1}{\sqrt{2}} C_A \rho g_{\text{eff}} q_{\text{sgs}}. \quad (8)$$

Here the effective gravity is more precisely defined by

$$g_{\text{eff}} = \chi_{\pm n\Delta}(G=0)\theta(\Delta - \lambda_{\text{fp}})\text{At}(\rho)g, \quad (9)$$

where $\chi_{\pm n\Delta}(G=0)$ is the characteristic function of all cells for which the distance from the flame front (represented by $G(\mathbf{x}, t) = 0$) is less than δ , and θ is the Heaviside step function, i.e. $\theta(\Delta - \lambda_{\text{fp}}) = 1$ for $\Delta > \lambda_{\text{fp}}$ and zero otherwise. The Atwood number is expressed as a function of the mean density which is obtained from a fit to the numerical data from Timmes & Woosley (1992):

$$\text{At}(\rho) = \frac{1}{2} \left[0.0522 + \frac{0.145}{\sqrt{\rho_9}} - \frac{0.0100}{\rho_9} \right] \quad (10)$$

The closure (8) does not include all of the intricate effects that contribute to SGS buoyancy. It merely captures what is presumably the leading order effect. In fact, one would have to model the interaction between turbulent potential and kinetic energy fluctuations on unresolved scales. Unfortunately, there exists no theoretical framework for this task yet. Moreover, the concept of a SGS Archimedian force entails a violation of energy conservation because the contribution of Γ_{sgs} to the production of turbulence energy is not balanced in the resolved energy budget. Consequently, the total energy of the system effectively increases. However, Γ_{sgs} is non-zero only in a small volume fraction. For this reason, the resulting violation of energy remains negligible relative to the total energy budget.

In order to determine the parameter C_A , we observe that the Sharp-Wheeler SGS model is obtained as an asymptotic relation in the limiting case of neglecting the non-local transport $\mathfrak{D}_{\text{sgs}}$, the turbulent energy transfer Σ_{sgs} and the pressure-dilatation λ_{sgs} (see Sect. 2 of paper I for definitions). Dropping the corresponding terms in equation (4), one obtains

$$\frac{D}{Dt} q_{\text{sgs}} \simeq \frac{1}{\sqrt{2}} C_A g_{\text{eff}} - \frac{q_{\text{sgs}}^2}{\ell_\epsilon}. \quad (11)$$

for a fluid parcel in the vicinity of the flame front. In the stationary regime, this equation has the fixed point solution:

$$q_{\text{sgs}} \simeq \sqrt{\frac{2C_A \Delta_{\text{eff}} g_{\text{eff}}}{C_\epsilon}} = v_{\text{RT}}(\Delta_{\text{eff}}). \quad (12)$$

Consistency with the Sharp-Wheeler relation (1) implies $C_A = C_\epsilon/8$. Since $C_\epsilon \approx 0.5 \dots 1.0$ for developed turbulence (see Schmidt et al. 2005a), the estimate $C_A \approx 0.1$ is obtained.

2.2. Rescaling of the subgrid scale turbulence energy

If a non-static, co-moving grid is used, the implicit filter $\langle \rangle_{\text{eff}}$ introduced in paper I, Sect. 3, becomes time-dependent. Therefore, time-derivates do not commute with the operation of filtering and additional terms arise in the dynamical equations. These terms are equivalent to the additional fluxes which are included in the implementation of the Riemann solver for moving grids (Müller 1994; Röpke 2005). However, there is a subtlety related to the shifting cutoff which separates the resolved and unresolved scales. As the grid expands homologously with the bulk of the white dwarf, the grid resolution Δ gradually decreases in time and the growing cutoff length entails a gradual rise of the SGS turbulence energy. This rise is inherent to the grid geometry and immediately affects the decomposition of the energy budget. The two-thirds law for developed turbulence implies $\langle q_{\text{sgs}} \rangle \propto \Delta^{1/3}$ (see Frisch 1995, Sect. 5). Thus, it is easy to rescale the mean value of q_{sgs} if Δ changes by a small fraction $\delta\Delta/\Delta$:

$$\langle q_{\text{sgs}}^{(1+\delta)\Delta} \rangle \propto \left(1 + \frac{1}{3} \frac{\delta\Delta}{\Delta} \right) \langle q_{\text{sgs}}^\Delta \rangle \quad (13)$$

Because this scaling law is a statistical rule one cannot expect that it holds locally. However, the dynamical procedure for the calculation of the eddy-viscosity also can be utilised for a

localised rescaling law. Let Δ_t be the grid resolution at time t , and $\Delta_{t-\delta t}$ the slightly smaller resolution prior to the last time step. Applying the test filter introduced in paper I, Sect. 4.1, at time t , the turbulent velocity q_T associated with velocity fluctuations on length scales greater than $\beta\Delta_t$ and smaller than $\gamma_T\beta\Delta_t$ is obtained. Here $\beta = \Delta_{\text{eff}}/\Delta$ is the constant ratio of the effective cutoff length to the size of the grid cells. Since the Riemann solver does not account for the fractional growth of the turbulence energy due to the shift of the cutoff, the result of advancing the dynamical equations from $t - \delta t$ to t is $q_{\text{sgs}}^{\Delta_{t-\delta t}}$. Now an estimate of $q_{\text{sgs}}^{\Delta_t}$ can be made locally via interpolation of the turbulence energy in length scale space. Using the contracted Germano identity (paper I, Sect. 4.1), the total turbulence energy associated with the test filter length at time t is given by

$$k_{\text{turb}}^{\gamma_T\Delta_t} = \frac{\langle \rho k_{\text{sgs}}^{\Delta_t} \rangle_T}{\rho^{(T)}} + k^{(T)}. \quad (14)$$

The unknown is the rescaled SGS turbulence energy $k_{\text{sgs}}^{\Delta_t}$. Neglecting compressibility effects and variations on sub-test filter lengths, we set $k_{\text{turb}}^{\gamma_T\Delta_t} \simeq k_{\text{sgs}}^{\Delta_t} + k^{(T)}$. Then linear interpolation between $\Delta_{t-\delta t}$ and $\gamma_T\Delta_t$ yields:

$$k_{\text{sgs}}^{\Delta_t} \simeq k_{\text{sgs}}^{\Delta_{t-\delta t}} + \frac{f}{1-f} k_T, \quad (15)$$

where the interpolating factor f is given by

$$f = \frac{\Delta_t - \Delta_{t-\delta t}}{\gamma_T\Delta_t - \Delta_{t-\delta t}}. \quad (16)$$

Due to the smallness of a CFL time step, the fractional changes of the cutoff length will be small. Hence, $f \ll 1$.

The problem with the rescaling law (15) is that it fails to account for the correct asymptotic behaviour in the limit of fully developed turbulence. On account of the Germano identity (paper I, Sect. 4.1), one would expect the statistical relation

$$(\gamma_T^{2/3} - 1) \langle k_{\text{sgs}} \rangle = \langle k^{(T)} \rangle \quad (17)$$

for regions of nearly homogeneous turbulence obeying Kolmogorov scaling. This relation is asymptotically reproduced by the rescaling modified law

$$k_{\text{sgs}}^{\Delta_t} \simeq \frac{\gamma_T^{2/3}(1-f)}{\gamma_T^{2/3}-f} k_{\text{sgs}}^{\Delta_{t-\delta t}} + \frac{f}{\gamma_T^{2/3}-f} k_T, \quad (18)$$

which results from the interpolation of the turbulence energy divided by the associated length to the power 2/3. This is the rescaling law which was implemented for the numerical simulations of thermonuclear supernova explosions discussed in the next section.

3. Numerical simulations

In the following, we will present results from several numerical simulations using the methodology outlined in Röpke & Hillebrandt (2005). In essence, the piece-wise parabolic method is used to solve the hydrodynamical equations (Colella & Woodward 1984; Fryxell et al. 1989) and the evolution of the flame-fronts is computed by means of the level

set method in the passive implementation (Osher & Sethian 1988; Reinecke et al. 1999). The implemented equation of state for electron-degenerate matter is described in Reinecke (2001), Sect. 3.2. Thermonuclear burning is modelled by simple representative reactions (Reinecke et al. 2002): ^{12}C and ^{16}O is fused to ^{56}Ni and α -particles at densities higher than $5.25 \cdot 10^7 \text{ g cm}^{-3}$, whereas ^{24}Mg is produced at lower densities in the late stage of the explosion. Finally, all reactions cease below 10^7 g cm^{-3} . This threshold presumably marks the transition from the flamelet to the broken reaction zone regime of turbulent burning (see Niemeyer & Kerstein 1997). The correct treatment of the burning process in this regime is still a matter of debate and, for this reason, not included in the present simulations.

As initial model, we choose a white dwarf of mass $M = 1.4M_\odot$ composed of equal mass fractions of carbon and oxygen with a central density $\rho_c = 2.0 \cdot 10^9 \text{ g cm}^{-3}$ and temperature $T_c = 7.55 \cdot 10^8 \text{ K}$. As suggested by Wunsch & Woosley (2004), the radial temperature profile is given by a parabola with a cutoff at the thermal radius $\Lambda = 7.35 \cdot 10^7 \text{ cm}$:

$$T(r) = T_c \left[1 - \left(\frac{r}{\Lambda} \right)^2 \right] \theta(r - \Lambda) + T_0 \theta(\Lambda - r), \quad (19)$$

where θ denotes the Heaviside step function. The thermal radius specifies the size of the convective core prior to the runaway. At larger radii, the matter is isothermal with $T_0 = 5 \cdot 10^5 \text{ K}$. In the centre, we set an axisymmetric initial burning region with sinusoidal perturbations (see Röpke & Hillebrandt 2005). In order to achieve higher resolution, only single octants subject to reflecting boundary conditions were evolved in the simulations discussed here.

Moreover, we applied the co-expanding grid technique of Röpke (2005). Thereby, it is possible to maintain an equidistant grid geometry over the whole domain of turbulent burning at any stage of the explosion, even when the ejecta have expanded by a large factor compared to the initial size of the white dwarf. Recently, Röpke et al. (2005) have combined this technique with the grid geometry used by Reinecke et al. (2002) in order to capture the burning process in the interior with optimal resolution, while using a coarser grid with exponentially increasing cells outside. The hybrid grid, even at moderate resolution, enables us to resolve details of the turbulent flame dynamics which used to be inaccessible for non-adaptive schemes. All numerical simulations presented in this article feature a hybrid grid.

The non-uniform grid geometry poses certain difficulties when applying the localised SGS model. In Sect. 2.2, we showed that it is relatively easy to account for the variation in the time domain due the co-expansion of the grid. In the case of non-uniform grids, however, the filter operation does not commute with spatial derivatives in the dynamical equations. Apart from that, the weighing of nodes for the discrete filtering procedure becomes dependent on the location. This would lead to substantial complications in the numerical implementation. Fortunately, we found a simple solution: Since the turbulent dynamics mostly takes place in the burning region which is contained within the uniform part of the grid, we computed the eddy-viscosity parameter C_ν only in this region and set the rate

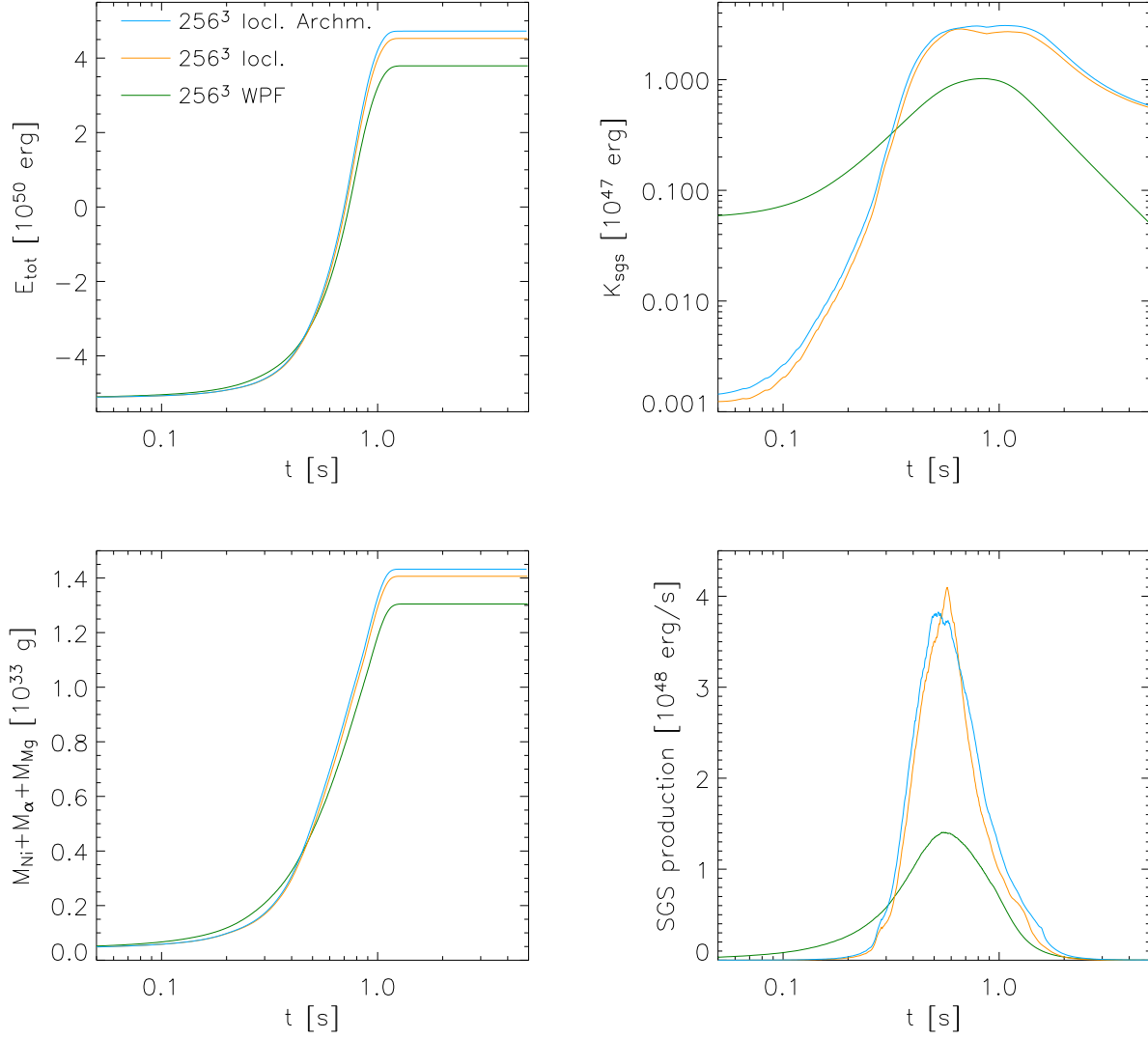


Fig. 1. Time evolution of integrated quantities for three simulations with identical initial conditions and resolution 256^3 . In one case, Clement’s SGS model with wall proximity functions (WPF) was used. For the other two simulations we applied the localised SGS model with Archimedian production, respectively, switched off and on.

of turbulent energy transfer equal to zero in the exterior. Later in this section, we will demonstrate that neglecting the energy transfer outside the burning region can be justified *a posteriori*.

The original SGS turbulence energy model implemented by Niemeyer & Hillebrandt (1995) is based on statistical closure parameters. Clement (1993) suggested to set $C_v = 0.1W$, where W is an empirical *wall proximity function* (WPF),

$$W = \min \left[100, \max \left(0.1, \cdot 10^{-4} \frac{e_{\text{int}}}{k_{\text{sgs}}} \right) \right]. \quad (20)$$

Since $e_{\text{int}} \sim c_s^2$, the ratio $e_{\text{int}}/k_{\text{sgs}}$ is basically an inverse Mach number squared. If there is little turbulence energy, C_v is considerably enhanced. On the other hand, C_v becomes smaller than 0.1 if the SGS turbulence velocity exceeds a few percent of the speed of sound. This behaviour of the eddy-viscosity parameter is qualitatively different from the prediction of the

dynamical procedure which implies less energy transfer if turbulence is still developing but enhanced transfer in the fully developed case (Schmidt et al. 2005a).

This is clearly reflected in the time evolution of the turbulence energy in two simulations which differ only in the SGS model. The graphs of the mass-integrated SGS turbulence energy are plotted in the top panel on the left of Fig. 1. There are two variants of the localised SGS model, one including Archimedian production as described in Sect. 2.1, whereas it is assumed that energy transfer through the cascade is the only source of turbulence production in the alternative model. In contrast to Clement’s model, there is initially very little SGS turbulence energy followed by a much steeper rise in the simulations with the localised SGS model. The rapid growth of turbulence energy can be attributed to the substantially stronger turbulence production within the time interval from 0.3 to 1.0 s

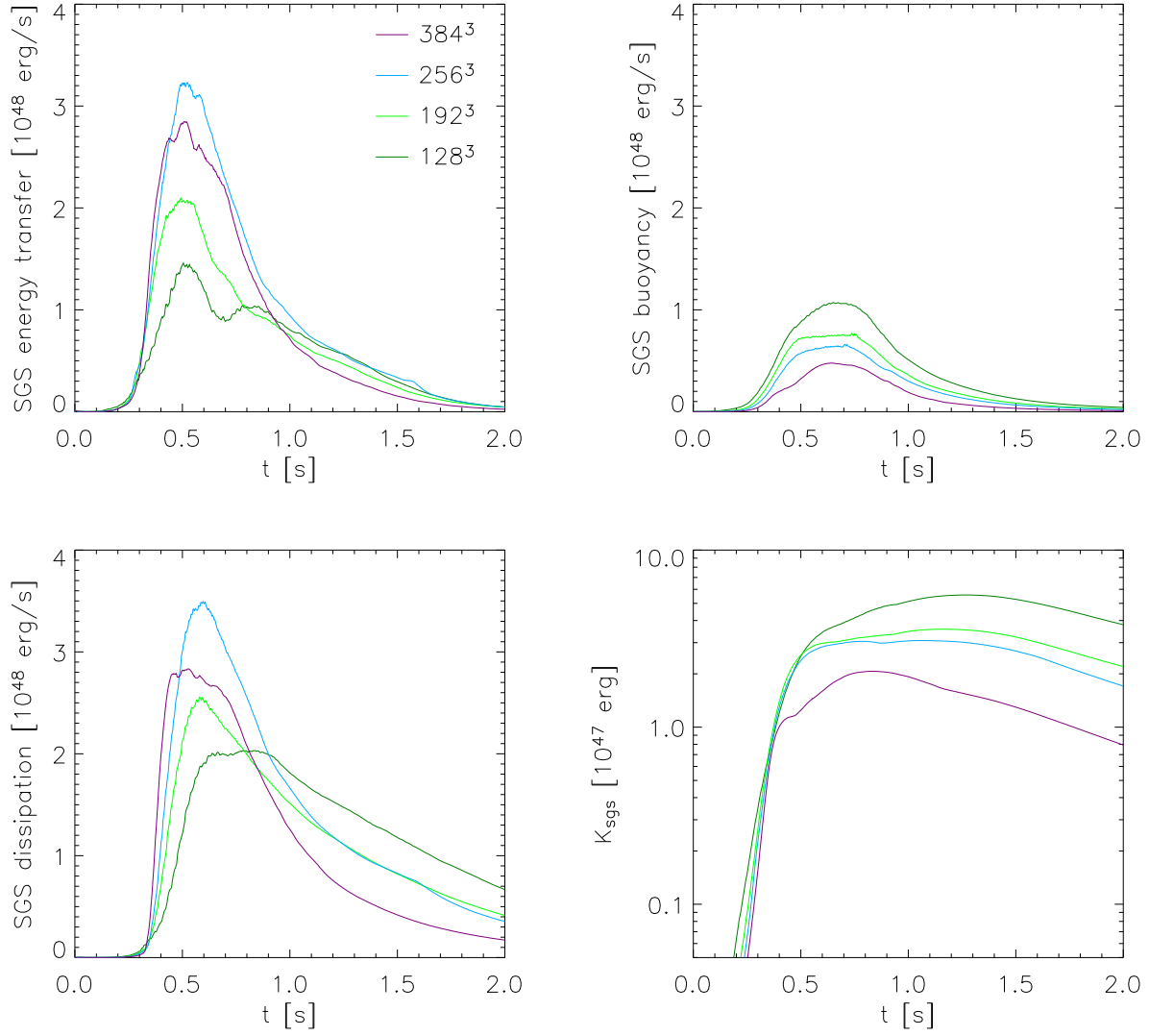


Fig. 2. Time evolution of integrated SGS quantities for a series of simulations with varying resolution.

(see right bottom panel in Fig. 1). In the second half of the combustion phase, the total SGS turbulence energy is almost one order of a magnitude larger which enhances the flame propagation speed accordingly. At later times, the discrepancy becomes even more pronounced because the rescaling of k_{sgs} implemented in the localised model feeds kinetic energy into the subgrid scales against the action of SGS dissipation. The net result is a significant enhancement of the explosion energy and a larger yield of burning products (see bottom panel on the left of Fig. 1). Also note that the additional production of SGS turbulence by the Archimedian force term in equation (4) increases the explosion energy even further. Compared to the reference simulation with Clement's model, the final kinetic energy of $0.472 \cdot 10^{51}$ erg is about 25 % greater. However, this does not imply that Archimedian production dominates over the turbulence cascade. In fact, the evolution of the SGS turbulence energy differs only little, as one can see from the plot in Fig. 1. In conclusion, SGS buoyancy effects appear to influence the

explosion but turbulent energy transfer from resolved scales is nevertheless the primary source of SGS turbulence production.

According to the scaling argument mentioned in the introduction, buoyancy should become even less important relative to the turbulent energy transfer with increasing resolution. This is indeed observed in a series of simulations with the resolution varying between 128^3 up to 384^3 grid cells. The time evolution of the integrated rate of energy transfer and specific Archimedian force, respectively, is plotted in the top panels of Fig. 2. In order to interpret these graphs, it is important to note that the SGS energy transfer is expected to become statistically scale invariant in the case of Kolmogorov turbulence. This follows from the scaling law $v'(l) \propto l^{1/3}$ for the turbulent velocity fluctuations. Hence, $k_{\text{sgs}} \propto \Delta^{2/3}$. Since the characteristic time scale of turbulent velocity fluctuations scales with $l^{2/3}$, it follows that the average time derivative of k_{sgs} is scale invariant. The rate of energy transfer per unit mass, on the other hand, is proportional to $\Delta k_{\text{sgs}}^{1/2} |S^*|^2$. This expression is

also scale-invariant because the rate-of-strain scalar $|S^*|$ measures the inverse time scale of the smallest resolved velocity fluctuations, i.e. $|S^*|^2 \propto \Delta^{-4/3}$, while $\Delta k_{\text{sgs}}^{1/2} \propto \Delta^{4/3}$. The computed rate of energy transfer plotted in the top panel on the left of Fig. 2 exhibit peak values which are within the same order of magnitude, although the energy transfer seems to be underestimated for the lowest resolutions. Initially, the turbulence energy rises exponentially at a rate which changes only little with resolution (right bottom panel in Fig. 2). This is reflected in the nearly coinciding graphs of the rate of SGS energy transfer up to $t \approx 0.3$ s shown in the left panel on the top of Fig. 2.

The SGS turbulence energy in the regime of fully developed turbulence decreases for higher resolution. This trend can be discerned particularly in the post-burning phase, in which no further energy is injected and the turbulent flow begins to decay. From the initial production phase to the post-burning phase, however, a rather complicated behaviour becomes manifest as the result of the interplay between turbulence production by the strain of the resolved flow, the SGS Archimedian force and the grid expansion. The explosion energetics plotted in Fig. 3 shows the following behaviour depending on the numerical resolution (also see Table 1): Whereas the final value of the total energy is about the same for the lower resolutions, there is a significantly enhanced yield of energy in the case $N = 384^3$. However, this does not imply that the model fails to converge with increasing resolution. Turbulent flow regions are confined in a fraction of the numerical grid, whereas the greater part of the grid is overhead required for modelling the non-turbulent outer parts of the expanding star and some portion of the surrounding quasi-vacuum. In the case $N = 256^3$, for example, significant SGS turbulence production occurs in the inner 100^3 cells at $t = 0.5$ s. This is the time of maximal integrated turbulence production. However, in paper I we demonstrated that 100 cells in each spatial dimension is definitely not sufficient to resolve developed turbulent flow sufficiently far down toward the inertial subrange using PPM. Although this is merely a crude estimate, it appears plausible that even the supernova simulation with $N = 384^3$ resolves the turbulent dynamics only marginally. As a further indication, the plateau-like flattening of the rate of production and dissipation, respectively, can be seen in the left panels of Fig. 2 for the highest resolution only. We interpret the flattening as a consequence of local statistical equilibrium between production and dissipation.

Unfortunately, we were not able to perform a run of still higher resolution due to the limitations of our computational resources. In any case, we expect that $N = 512^3$ grid cells in one octant would be sufficient for an accurate modelling of the turbulent dynamics, whereas simulations with less resolution can be utilised to discern trends in parameter studies. A similar conclusion was drawn by Röpke (2005) from a series of two-dimensional simulations, in which a pronounced jump of the total energy was found between the $N = 256^2$ and the 512^2 run, respectively, while more or less the same energy was obtained for $N \geq 512^2$. Moreover, snapshots of the zero level set for varying resolution suggested that secondary Kelvin-Helmholtz instabilities are barely or not at all resolved with $N \leq 256^2$.

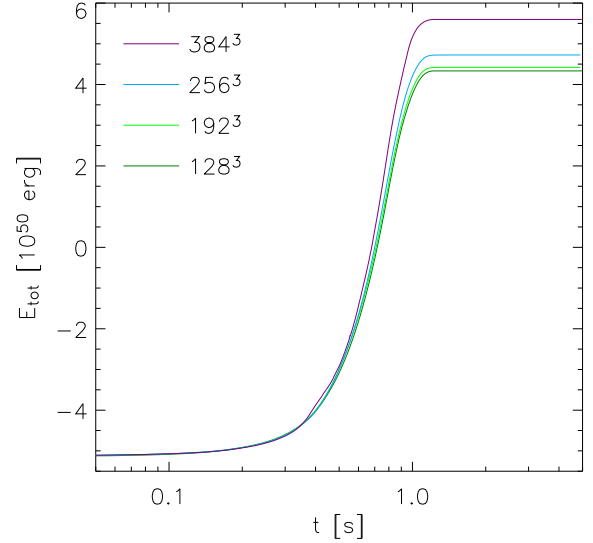


Fig. 3. Time evolution of the total energy for the same simulations as in Fig. 2

Table 1. Total release of nuclear and kinetic energy and total masses of iron group (“Ni”) and intermediate mass (“Mg”) elements corresponding to Fig. 3.

N	$E_{\text{nuc}} [10^{51} \text{ erg}]$	$E_{\text{kin}} [10^{51} \text{ erg}]$	M_{Ni}/M_{\odot}	M_{Mg}/M_{\odot}
128^3	0.963	0.433	0.523	0.175
192^3	0.970	0.442	0.529	0.172
256^3	1.000	0.472	0.548	0.172
384^3	1.087	0.560	0.586	0.206

Details of the SGS dynamics are illustrated by contour plots of two-dimensional spatial sections from the simulation with $N = 384^3$ grid cells (Figs. 4, 5, and 6). In each Fig., the following dynamical terms of equation (4) are plotted:

1. Rate of production caused by strain, $\ell_v |S^*|^2$ (left top panel).
2. Specific Archimedian force $0.1 g_{\text{eff}}$ (right top panel).
3. Rate of dissipation $-\frac{7}{30} q_{\text{sgs}} d - q_{\text{sgs}}^2 / \ell_{\epsilon}$ (left bottom panel).
4. Rate of diffusion $\frac{1}{\rho} \nabla \cdot (\rho \ell_{\kappa} q_{\text{sgs}} \nabla q_{\text{sgs}}) - \ell_{\kappa} |\nabla q_{\text{sgs}}|^2$ (right bottom panel).

The flame surface as given by the zero level set is indicated by the contours in white. Note that these quantities have the dimension of acceleration. Fig. 4 shows the typical Rayleigh-Taylor mushroom shapes which have formed out of the initial sinusoidal perturbations at time $t = 0.3$ s. Significant energy transfer is concentrated in small regions and there is little dissipation yet. Comparing to Fig. 2, one can see that turbulence production is just about to rise. At $t = 0.45$ s, the rate of energy transfer has reached its maximum and is spread all over the interior of the flames (see Fig. 5). The acceleration of SGS fluid parcels subject to the largest strain exceeds 10^6 times the gravitational acceleration on Earth relative to the resolved flow. The

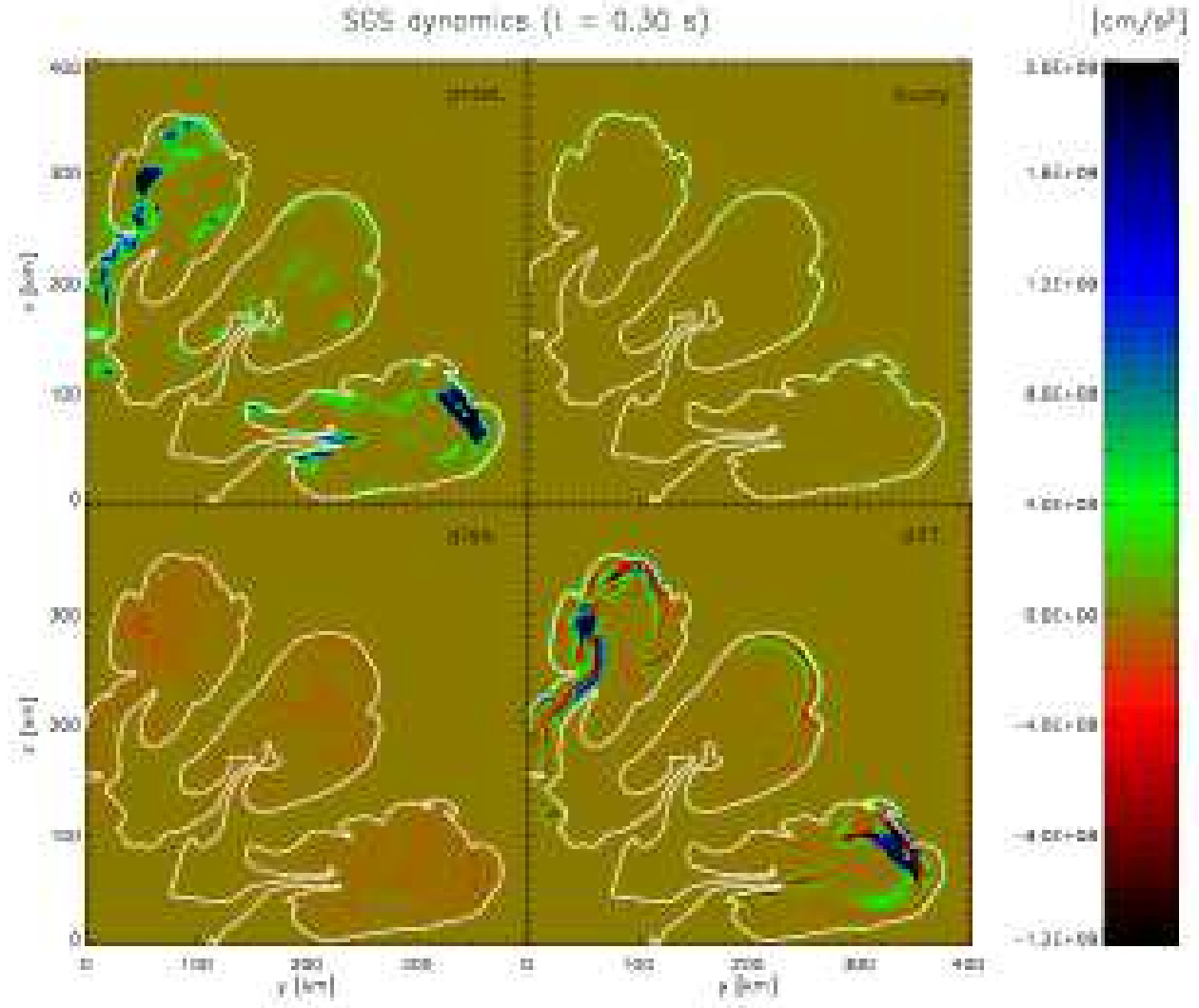


Fig. 4. Contour sections showing the contributions to the evolution of the SGS turbulence velocity q_{sgs} given by equation (4) at $t = 0.3$ s. Only the inner region of the grid with $N = 384^3$ cells is shown. The white contours represent the sections through the flame surface.

SGS buoyancy is typically by an order of a magnitude smaller. Both dissipation and transport due to SGS turbulent diffusion are comparable to the rate of energy transfer at this time. In the unburned material outside, on the other hand, there is virtually no SGS turbulence. Thereby, it is confirmed that switching off the energy transfer terms in the non-uniform grid regions at sufficient distance from the flame fronts is a reasonable simplification. Obviously, the flow is highly anisotropic in the vicinity of the flames which highlights the necessity of a localised SGS model. In Fig. 6, one can see that turbulent energy transfer is declining and becoming small relative to the Archimedian force near the flame front. However, this does not imply that the amount of SGS turbulence and, thus, the turbulent flame speed is dominated by the SGS buoyancy because the bulk of SGS turbulence energy has been produced by transfer of ki-

netic energy through the turbulence cascade and diffusion acts to redistribute this energy into regions with little production.

Fig. 10 shows the evolution of the SGS turbulence velocity q_{sgs} at the flame fronts in three-dimensional visualisations. The grid lines roughly indicate the uniform part of the numerical grid. The corresponding absolute scale is indicated by the size X_{uni} and the corresponding number of cells N_{uni} . In the first three snapshots one can see the growth of the initial perturbations. The axial symmetry is gradually broken by the formation of secondary instabilities. At $t = 0.45$ s the smaller plumes originating from these instabilities are highly turbulent. From $t = 0.6$ s onwards, the system increasingly loses its memory of the initial condition and the turbulence intensity at the flame surface is abating and levelling. The last snapshot at $t = 1.5$ s shows a complex structure with features over a wide range of

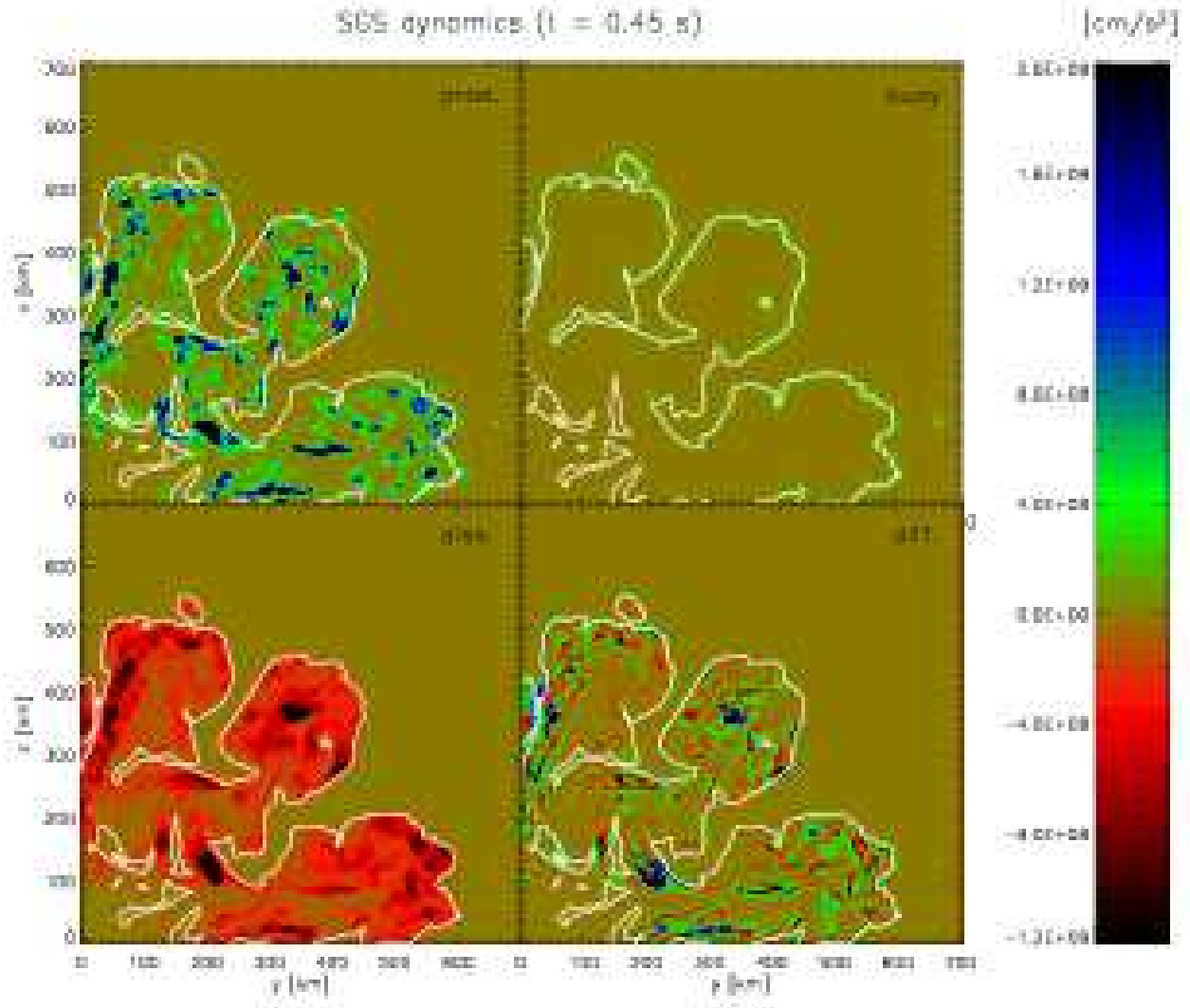


Fig. 5. The same plot as in Fig. 4 at $t = 0.45$ s.

scales. There appear to be five or six major modes which eventually prevail. The resulting layering of nuclear species is illustrated by the contour plots of the corresponding mass densities in Fig. 7. Nickel is concentrated in the central region, whereas both magnesium and unburned carbon and oxygen are found further outside. The outermost layers and the narrow down-drafts between the convective fingers of nuclear ash are composed almost exclusively of carbon and oxygen. The stratification of the nuclear species in the explosion ejecta is reflected in the corresponding mass density functions dM/dv_r , where v_r is the radial velocity component. In particular, Fig. 8 shows that little carbon and oxygen is found for velocities less than 3000 km s^{-1} in the late phase of almost homologous expansion.

To understand the flame dynamics, it is instructive to consider the probability density function (PDF) of the logarithm of the flame propagation speed s_t over the surface of the flame. The PDFs for several instants of time are plotted in Fig. 9.

Note that integrating each PDF over the decade logarithm of the speed yields unity. Also shown are the PDFs of q_{sgs} and $v_{\text{RT}}(\Delta_{\text{eff}})$. The relation between the turbulent flame speed s_t and the SGS turbulence velocity q_{sgs} is formulated in equation (2). During the first tenth of a second, s_t is basically given by the laminar flame speed. Then the flame propagation becomes increasingly affected by SGS turbulence. From about 0.3 s onwards, s_t is dominated by q_{sgs} . At later times, one can see the asymptotic relation $s_t \simeq 2q_{\text{sgs}}/\sqrt{3}$. The Rayleigh-Taylor velocity scale $v_{\text{RT}}(\Delta_{\text{eff}})$ is initially much smaller than the laminar burning velocity. As the flame propagates outwards, both the gravity and the density contrast at the flame surface become larger and $v_{\text{RT}}(\Delta_{\text{eff}})$ increases. Eventually, the PDF of $v_{\text{RT}}(\Delta_{\text{eff}})$ tends toward a rather narrow peak around 10^7 cm s^{-1} . The PDF of q_{sgs} , on the other hand, extends over a substantially wider range. For this reason, the localised SGS model generates more variation in the propagation of the flame front in comparison to

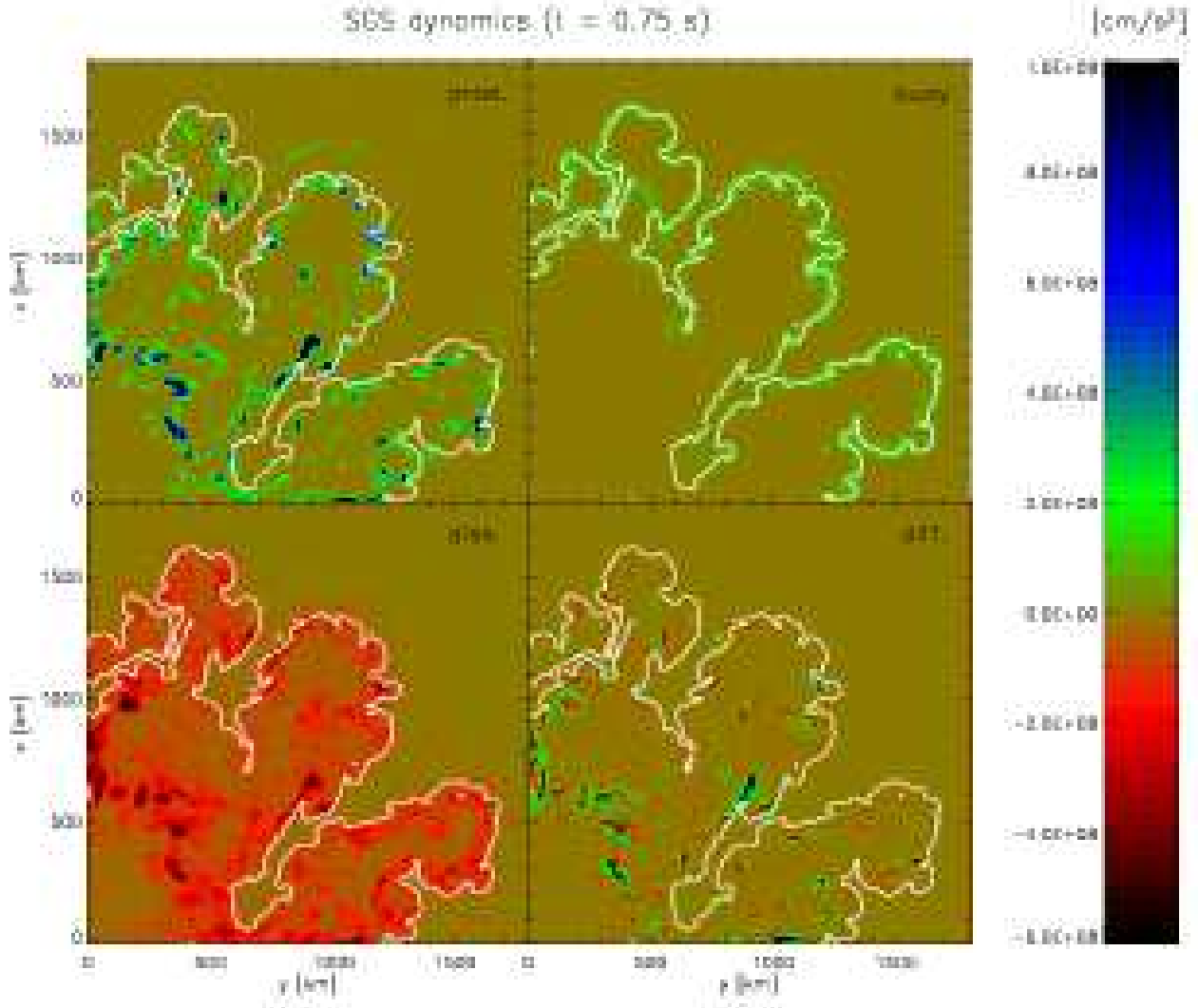


Fig. 6. The same plot as in Fig. 4 at $t = 0.75$ s.

the Sharp-Wheeler model. This is expected because the Sharp-Wheeler relation is ignorant of the interaction between sub-grid and resolved scales and the effects of non-local transport. Nevertheless, $v_{RT}(\Delta_{eff})$ is seemingly a velocity scale which is representative for the magnitude of q_{sgs} at the flame surface during most of the burning process.

4. Conclusion

We applied the SGS turbulence energy model to the large eddy simulation of turbulent deflagration in thermonuclear supernova explosions. The novel features of this model are a localised closure for the rate of energy transfer, an additional Archimedian force term which accounts for buoyancy effects on unresolved scales and the rescaling of the SGS turbulence energy due to the shift of the cutoff length in simulations with a co-expanding grid. We found that the production of turbulence is largely confined to the regions near the flame fronts and

in the interior ash regions. Consequently, there is pronounced anisotropy at the flame surface which can be tackled by the localised SGS model only. The Archimedian force contributes noticeably to the turbulent flame speed, particularly once the flame surface has grown substantially. However, the dominating effect is the energy transfer through the turbulence cascade. In the late stage of the explosion, sustained turbulence energy comes from the rescaling, while the major dynamical contribution is SGS dissipation. Furthermore, it appears that numerical grids with more than $N = 256^3$ cells in one octant are necessary in order to sufficiently resolve the turbulent dynamics in the burning regions and to obtain converged results.

An investigation of probability density functions over the flame fronts (see Fig. 9) reveals that the Rayleigh-Taylor velocity scale $v_{RT}(\Delta_{eff})$ given by the Sharp-Wheeler relation (1) is not negligible compared to the SGS turbulence velocity q_{sgs} , once the regime of fully turbulent burning has been en-

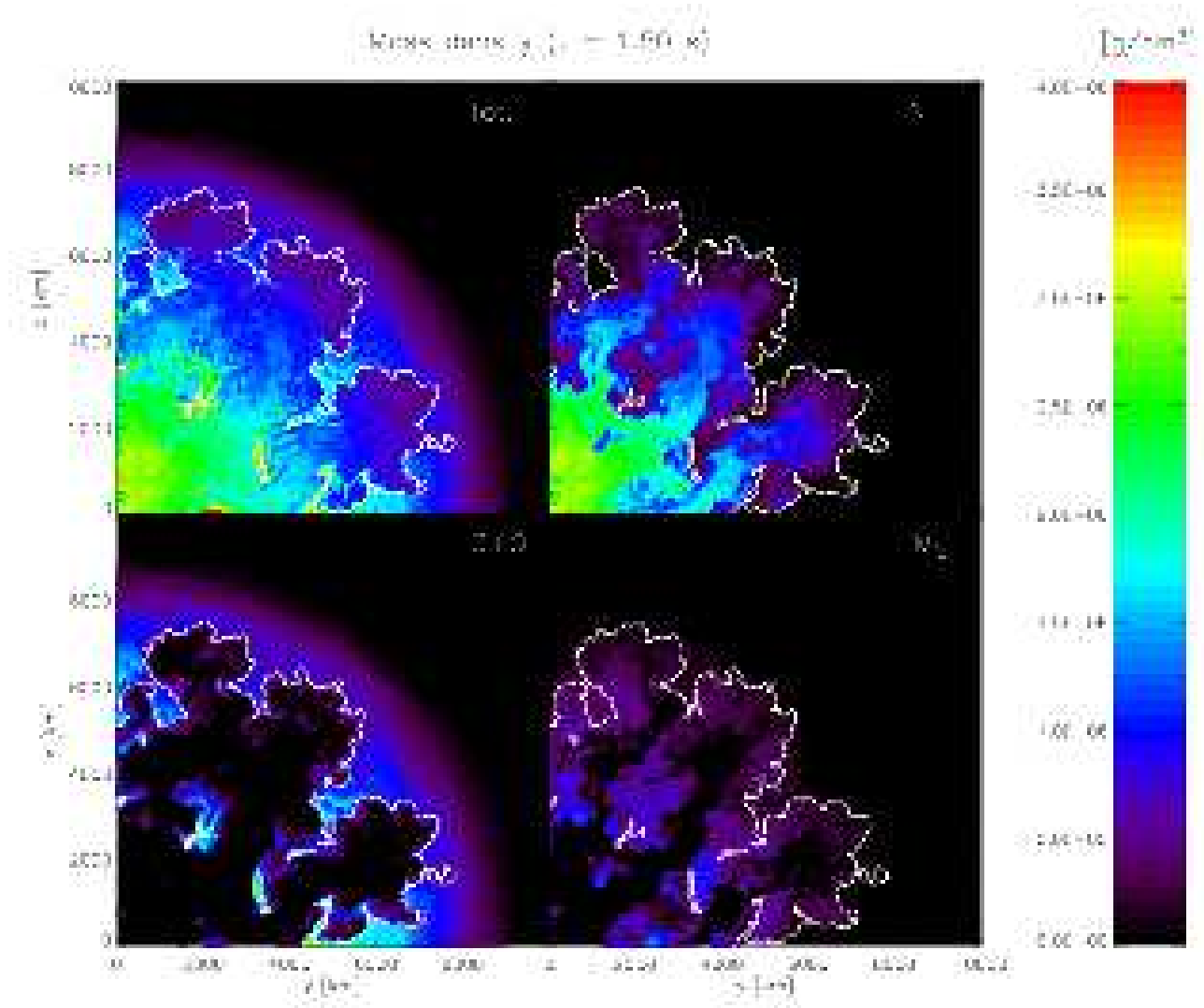


Fig. 7. Total and partial mass densities for the same simulation as in at Fig. 4–6 at $t = 1.5$ s.

tered. This reflects the slow decrease of the ratio $v_{\text{RT}}(\Delta_{\text{eff}})/q_{\text{sgs}}$ with the numerical cutoff scale according to the scaling argument discussed in the introduction. The underlying scaling relations do not necessarily apply to transient and inhomogeneous flows as in the supernova explosion scenario. The PDF for q_{sgs} shows a considerably wider spread than the sharply peaked PDF for $v_{\text{RT}}(\Delta_{\text{eff}})$. We interpret this observation as a consequence of the additional physics in the localised SGS model, which also encompasses turbulent energy transfer (i.e. interaction between resolved and subgrid scales) and turbulent transport (i.e. non-local interactions among subgrid scales). The relation between the Sharp-Wheeler and the turbulence energy models may be analogous to the relation between the mixing length and Reynolds stress models of convection.

The final kinetic energy in the simulation with the highest resolution is about $6 \cdot 10^{50}$ erg. The produced mass of iron group elements, $0.58M_{\odot}$, falls within the range deduced

from observations of type Ia supernovae (Leibundgut 2000). However, some observed events are substantially more energetic. Regarding the numerical simulations, the explosion energy is very sensitive to the initial conditions and the localised SGS model appears to increase the sensitivity even further. Using initial conditions that are different to the highly artificial centrally ignited flame is in progress. A persistent difficulty is the large amount of left over carbon and oxygen (see Fig. 7 and 8). It is not clear yet to what extent this problem can be solved with the aid of the localised SGS model in simulations with more realistic ignition scenarios. It appears more likely that a different mode of burning is required in the late explosion phase. The currently implemented numerical burning extinction at a density threshold of 10^7 g cm^{-3} is mostly arbitrary and should be replaced by a physical criterion motivated by the properties of distributed burning at low densities. This might turn out to be an alternative to the DDT scenario.

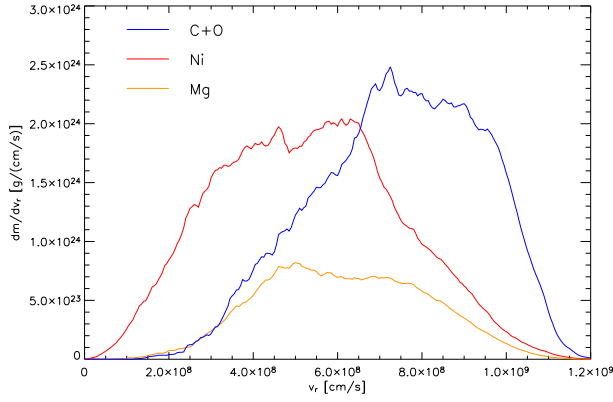


Fig. 8. Density functions of mass in radial velocity space for the major nuclear species in the same simulation as in Fig. 4–7 at $t = 5.0$ s.

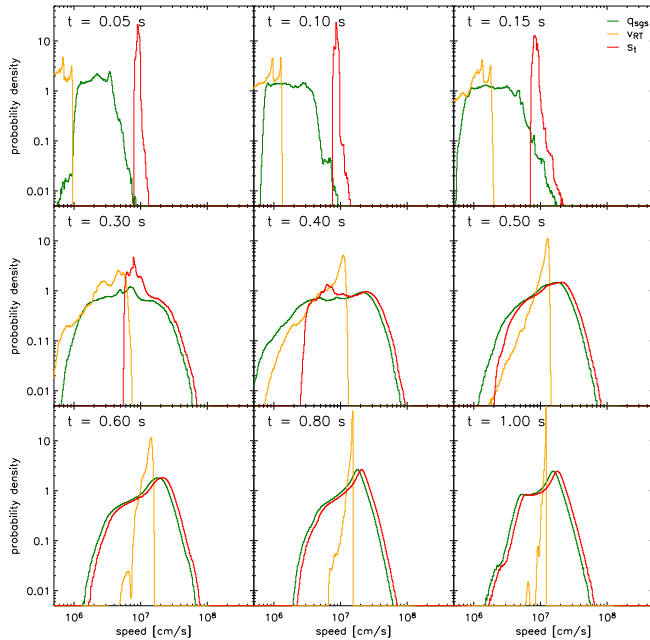


Fig. 9. Probability density functions of $v_{RT}(\Delta_{eff})$, q_{sgs} and s_t over the flame surface at several instants of time.

Acknowledgements. The numerical simulations were run on the Hitachi SR-8000 of the Leibniz Computing Centre in Munich and the IBM p690 of the Computing Centre of the Max-Planck-Society in Garching, Germany. The research of W. Schmidt and J. C. Niemeyer was supported by the Alfried Krupp Prize for Young University Teachers of the Alfried Krupp von Bohlen und Halbach Foundation.

References

Calder, A. C., Plewa, T., Vladimirova, N., et al. 2003, American Astronomical Society Meeting Abstracts, 203,
 Clement, M. J. 1993, *Astrophys. J.*, 406, 651
 Colella, P. & Woodward, P. R. 1984, *J. Comp. Physics*, 54, 174

Davies, R. M. & Taylor, G. 1950, *Proc. Roy. Soc. London A*, 200, 375
 Frisch, U. 1995, *Turbulence* (Cambridge University Press)
 Fryxell, B. A., Müller, E., & Arnett, W. D. 1989, *Hydrodynamics and nuclear burning*, MPA Green Report 449, Max-Planck-Institut für Astrophysik, Garching
 Gamezo, V. N., Khokhlov, A. M., & Oran, E. S. 2004, *Physical Review Letters*, 92, 211102
 Gamezo, V. N., Khokhlov, A. M., & Oran, E. S. 2005, *ApJ*, 623, 337
 Gamezo, V. N., Khokhlov, A. M., Oran, E. S., Chetchevanova, A. Y., & Rosenberg, R. O. 2003, *Science*, 299, 77
 Golombek, I. & Niemeyer, J. C. 2005, *A&A*, 438, 611
 Hoyle, F. & Fowler, W. A. 1960, *Astrophys. J.*, 132, 565
 Khokhlov, A. M. 1991, *Astron. & Astrophys.*, 245, 114
 Khokhlov, A. M., Oran, E. S., & Wheeler, J. C. 1997, *ApJ*, 478, 678
 Kim, W., Menon, S., & Mongia, H. C. 1999, *Combust. Sci. and Tech.*, 143, 25
 Leibundgut, B. 2000, *The Astron. Astrophys. Rev.*, 10, 179
 Müller, E. 1994, *Lecture Notes in Physics*, Vol. 433, *Galactic Dynamics and N-Body Simulations* (Springer-Verlag), 313–363
 Niemeyer, J. C. 1999, *Astrophys. J.*, 523, L57
 Niemeyer, J. C. & Hillebrandt, W. 1995, *Astrophys. J.*, 452, 769
 Niemeyer, J. C. & Kerstein, A. R. 1997, *New Astronomy*, 2, 239
 Niemeyer, J. C. & Woosley, S. E. 1997, *ApJ*, 475, 740
 Osher, S. & Sethian, J. A. 1988, *J. Comp. Phys.*, 79, 12
 Peters, N. 1999, *J. Fluid Mech.*, 384, 107
 Pocheau, A. 1994, *Phys. Rev. E*, 49, 1109
 Röpke, F. K. 2005, *A&A*, 432, 969
 Röpke, F. K. & Hillebrandt, W. 2005, *A&A*, 431, 635
 Röpke, F. K., Hillebrandt, W., Niemeyer, J. C., & Woosley, S. E. 2005, submitted to *A&A*. Preprint astro-ph/0510474
 Reinecke, M., Hillebrandt, W., & Niemeyer, J. C. 2002, *Astron. & Astrophys.*, 386, 936
 Reinecke, M., Hillebrandt, W., Niemeyer, J. C., Klein, R., & Gröbl, A. 1999, *Astron. & Astrophys.*, 347, 724
 Reinecke, M. A. 2001, PhD thesis, Department of Physics, Technical University of Munich, online available from <http://tumb1.biblio.tu-muenchen.de/publ/diss/ph/2001/reinecke.html>
 Schmidt, W., Hillebrandt, W., & Niemeyer, J. C. 2005a, *Combust. Theory Modelling*, 9, 693
 Schmidt, W., Hillebrandt, W., & Niemeyer, J. C. 2005b, *Comp. Fluids*, in press. Preprint astro-ph/0407616
 Schumann, U. 1975, *J. Comp. Physics*, 18, 376
 Sharp, D. H. 1984, *Physica D*, 12, 3
 Timmes, F. X. & Woosley, S. E. 1992, *Astrophys. J.*, 396, 649
 Woosley, S. E. & Weaver, T. A. 1994, *ApJ*, 423, 371
 Wunsch, S. & Woosley, S. E. 2004, *ApJ*, 616, 1102
 Zingale, M., Woosley, S. E., Rendleman, C. A., Day, M. S., & Bell, J. B. 2005, submitted to *ApJ*, preprint astro-ph/0501655

fig_c3_3d_015.png

(a) $t = 0.15$ s, $N_{\text{uni}} = 225^3$, $X_{\text{uni}} = 320$ km

fig_c3_3d_030.png

(b) $t = 0.3$ s, $N_{\text{uni}} = 242^3$, $X_{\text{uni}} = 484$ km

fig_c3_3d_045.png

(c) $t = 0.45$ s, $N_{\text{uni}} = 258^3$, $X_{\text{uni}} = 721$ km

fig_c3_3d_060.png

(d) $t = 0.6$ s, $N_{\text{uni}} = 283^3$, $X_{\text{uni}} = 1260$ km

fig_c3_3d_075.png

(e) $t = 0.75$ s, $N_{\text{uni}} = 308^3$, $X_{\text{uni}} = 2190$ km

fig_c3_3d_150.png

(f) $t = 1.5$ s, $N_{\text{uni}} = 340^3$, $X_{\text{uni}} = 9120$ km

Fig. 10. Evolution of the flames in the simulation with $N = 384^3$ grid cells. The colour shading indicates the value of q_{sgs} on a logarithmic scale.